Chemical Engineering Journal 475 (2023) 146428

Contents lists available at ScienceDirect

Chemical Engineering Journal

journal homepage: www.elsevier.com/locate/cej

Solvothermally silver doping boosting the thermoelectric performance of polycrystalline Bi_2Te_3

Wen-Yi Chen [a,b], Xiao-Lei Shi [b,*], Qishuo Yang [a,b], Meng Li [b], Wanyu Lyu [b], Ting Liu [a], Tianyi Cao [b], Boxuan Hu [b], Weidi Liu [c,b], Shuai Sun [d,b], Yuanqing Mao [a,b], Matthew Dargusch [a], Jin Zou [a,e], Zhi-Gang Chen [b,*]

[a] School of Mechanical and Mining Engineering, The University of Queensland, Brisbane, Queensland 4072, Australia
[b] School of Chemistry and Physics and Centre for Materials Science, Queensland University of Technology, Brisbane, Queensland 4000, Australia
[c] Australian Institute for Bioengineering and Nanotechnology, The University of Queensland, Brisbane, Queensland 4072, Australia
[d] Centre for Future Materials, University of Southern Queensland, Springfield Central, Queensland 4300, Australia
[e] Centre for Microscopy and Microanalysis, The University of Queensland, Brisbane, Queensland 4072, Australia

ARTICLE INFO

Keywords:
Thermoelectric
Bi_2Te_3
Solvothermal
Doping
Nanostructure

ABSTRACT

Bismuth telluride (Bi_2Te_3) is one of the most promising thermoelectric materials for commercial application at room temperature, but the thermoelectric performance of these materials still needs to be improved. In this study, we report a type of solvothermally Ag-doped Bi_2Te_3 microplate. By sintering these microplates into polycrystalline bulk materials, a high room-temperature figure of merit of 1 has been achieved. Based on comprehensive micro/nanostructural characterizations, we found that the solvothermally doped Ag in Bi_2Te_3 plays two main roles, namely as the dopants that effectively induce the point defects of Ag_{Bi} and forming Ag_2Te nanophases. Ag_{Bi} can provide additional hole charge carriers, effectively adjusting the initially high electron carrier concentration in the system, while the Ag_2Te nanophases effectively trigger energy filtering effect to maintain a high Seebeck coefficient, thereby contributing to a competitively high power factor of 25.5 μW cm^{-1} K^{-2} at 298 K. Simultaneously, a low thermal conductivity of 0.74 W m^{-1} K^{-1} is obtained due to the strong phonon scattering at various lattice imperfections, induced by the solvothermally Ag-doping, which include point defects, grain/phase boundaries, local lattice distortions, and dislocations. This work fills the gap in knowledge on the solvothermally Ag-doping mechanism in Bi_2Te_3 and provides guidance for the innovative design of high-performing inorganic thermoelectrics.

1. Introduction

With the continued growth of the semiconductor industry and portable electronics, the issue of heat dissipation has become a critical issue in limiting performance and lifespan. Thermoelectric devices are a more advantageous option than traditional vapor-compression refrigeration because of their smaller size, no moving parts or liquid, quick response time, longer lifespan, and silent operation [1]. However, the cooling efficiency of thermoelectric applications is limited by the performance of thermoelectric materials, which is determined by the dimensionless figure-of-merit $ZT = S^2\sigma T/\kappa$ [2], where S, σ, $S^2\sigma$, T, and κ are the Seebeck coefficient, electrical conductivity, power factor, absolute temperature, and thermal conductivity [3–5], respectively. κ is determined by the lattice thermal conductivity (κ_l) and electronic thermal conductivity (κ_e) [6,7]. To achieve a high ZT, it is necessary to secure a higher $S^2\sigma$ and lower κ [8]. However, the complicated interrelation among these parameters is a significant obstacle to improving overall efficiency [8,9]. Till now, much effort has focused on enhancing $S^2\sigma$ through band engineering or reducing κ_l through nanostructure engineering [8,10]. Benefiting from advanced strategies developed in recent years, many new thermoelectric materials have been developed with high experimental ZTs of > 2, such as Cu_2Se [11,12], SnSe [13–15], GeTe [16–18], and PbTe [19–21]. However, these materials mainly focus on applications at high temperatures (usually $>$ 500 K) [14]. Considering that many thermoelectric applications (*e.g.*, wearable thermoelectrics) [22–27] are based on the near-room-temperature region, developing high-performing near-room-temperature thermoelectric materials is still of significance.

* Corresponding authors.
E-mail addresses: xiaolei.shi@qut.edu.au (X.-L. Shi), zhigang.chen@qut.edu.au (Z.-G. Chen).

https://doi.org/10.1016/j.cej.2023.146428
Received 20 July 2023; Received in revised form 12 September 2023; Accepted 2 October 2023
Available online 5 October 2023

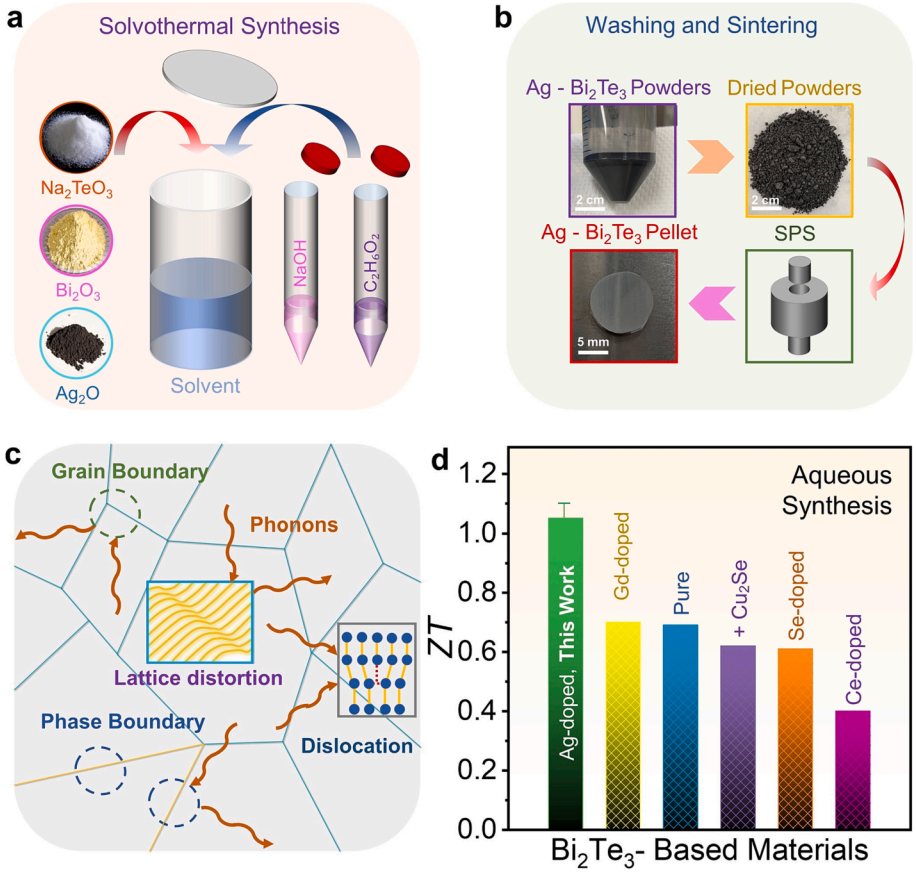

Fig. 1. Introduction of solvothermally doping Ag in n-type Bi_2Te_3 and its competitive thermoelectric performance. (a) Schematic diagram of the solvothermal route to synthesize Ag-doped Bi_2Te_3. (b) Photos of as-synthesized Ag-doped Bi_2Te_3 powders and subsequent washing, drying, and sintering processes. (c) Illustration of crystal/lattice imperfections observed in Ag-doped Bi_2Te_3 bulk materials. (d) Comparison of ZT values at room temperatures between this work and reported studies based on solvothermal synthesis routes [32,45,57–59].

Bismuth telluride (Bi_2Te_3) is one of the most promising thermoelectric materials that can be used at near-room temperatures since Bi_2Te_3 possesses intrinsically decent σ and S due to its narrow bandgap (~0.15 eV) with high valley degeneracy and anisotropic effective mass [28,29]. Therefore, both n- and p-type Bi_2Te_3-based thermoelectric materials have been widely employed in various commercial applications for thermoelectric power generation and solid-state cooling [9,30]. To improve the energy conversion efficiency and broaden their applications, their ZT values at near-room temperatures still need to be improved [14]. To achieve this goal, developing new strategies is of importance [20]. Among all developed strategies, doping based on band engineering is regarded as one of the most effective methods to improve $S^2\sigma$ and reduce κ_l through inducing point defects since rational point defects can tune the carrier concentration n to an appropriate value and strengthen the phonon scattering caused by the as-induced lattice distortions [7,31]. Till now, many doping methods have been investigated to further enhance the thermoelectric performance of Bi_2Te_3 through alloying with elements (*e.g.*, Ce, Cu, Gd, Ge and Ag) by melting or mechanical alloying routes [32–37], and the highest ZTs for n-type Bi_2Te_3 have reached ~ 1.4 at room temperature [36,37]. Besides that, there are some classic Bi_2Te_3-based materials contain $Bi_2Te_{3-x}Se_x$ [38–40] and $(Bi_2Te_3)_{1-x}(Bi_2Se_3)_x$ [41,42], which the highest ZT can reach 1.2 [39,40] and 0.71 [41,42] at near-room-temperature, respectively. In addition to doping, alloying with secondary phases especially nanophases is another effective strategy to improve S while maintaining a high σ by energy filtering effects [14], and designing multidimensional nano/microscale crystal or lattice imperfections is effective to suppress κ_l due to the strengthened phonon scattering at these sources [15]. Therefore, to achieve a high ZT in Bi_2Te_3, comprehensive strategies should be considered, and the fabrication route to achieve this goal should be facile but effective.

Till now, there have been many synthesis techniques developed for fabricating thermoelectric Bi_2Te_3, including zone-melting [43,44], ball milling [40,44], and solution-based synthesis such as hydrothermal/solvothermal methods [31,39,40,43–46]. Among these fabrication routes, the hydrothermal/solvothermal method is a facile method to synthesize the Bi_2Te_3 powders with significant anisotropy to further improve the thermoelectric performance [31,46,47]. Except for the texturing, the cation and anion vacancy concentrations can be easily controlled according to the chemical kinetics and thermodynamics by adjusting the stoichiometric ratio of precursors, synthesis temperature and pressure, and potential of hydrogen (pH) level [7,48,49]. Compared with other methods, hydrothermal/solvothermal methods are usually cost-effective with low energy consumption [14], and can usually achieve the comprehensive strategies discussed above *via* a one-step route [14]. However, although there have been numerous reports on conventional doping processes for Bi_2Te_3, most of these reports are primarily based on materials prepared using melting or solid-state solution methods [50–52]. In the case of Bi_2Te_3 prepared using a solvothermal/hydrothermal method, the doping mechanisms are different due to variations in the preparation process [53,54]. Furthermore, prior research efforts that attempted solvothermal doping often lacked detailed electron microscopy characterization to investigate the doping mechanisms thoroughly [50–52]. Therefore, our work aims to effectively fill this gap in the existing literature. Also, hydrothermal/solvothermal synthesis routes for Bi_2Te_3 still have considerable potential to be investigated to further improve their thermoelectric performance.

In this work, we design a facile solvothermal synthesis method to

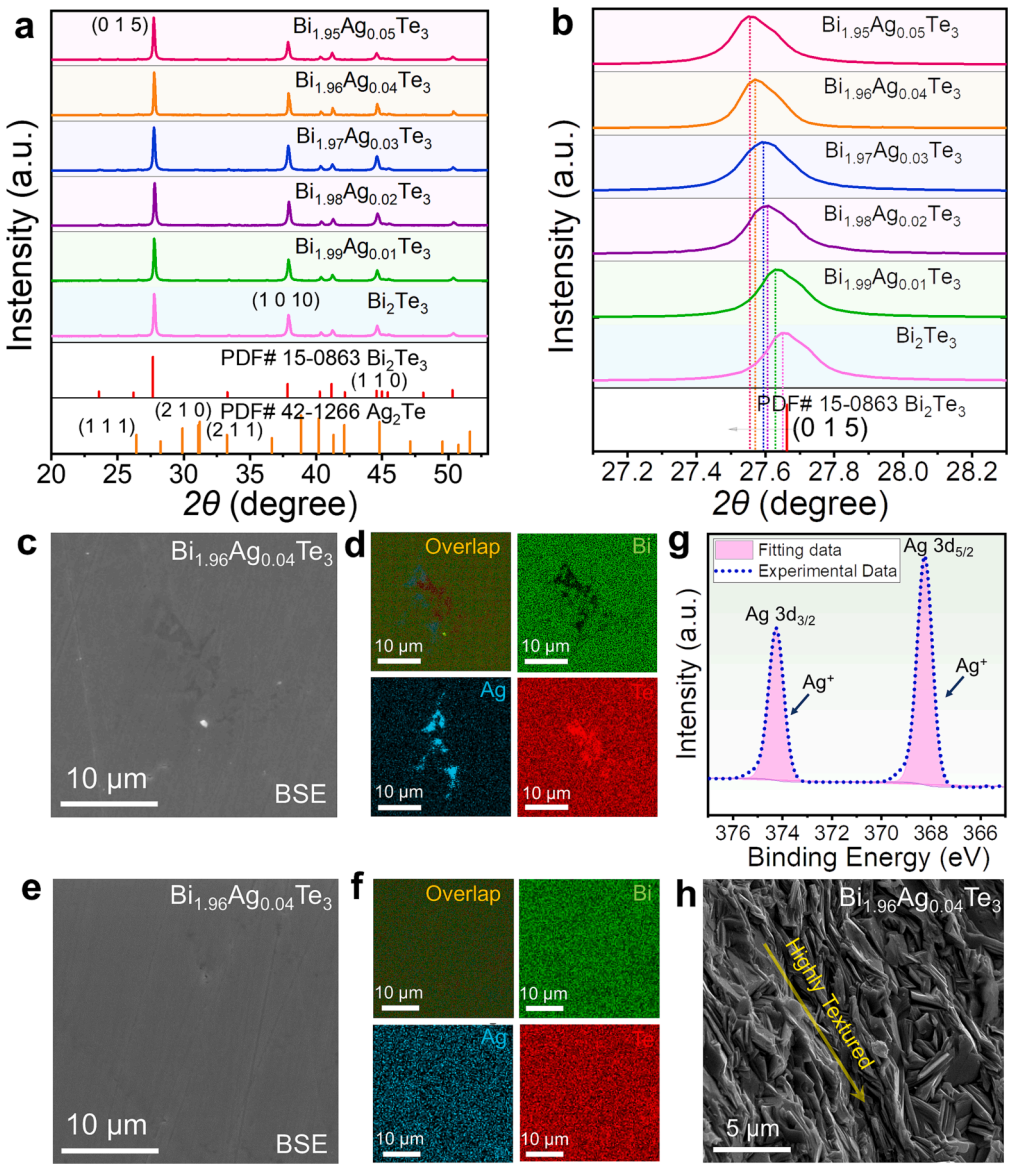

Fig. 2. Characterizations of phase and structure information of solvothermally synthesized Ag-doped Bi_2Te_3: (a) X-ray diffraction (XRD) patterns of $Bi_{2-x}Ag_xTe_3$ (x = 0, 0.01, 0.02, 0.03, 0.04, and 0.05) pellet samples. (b) Corresponding magnified XRD patterns of the (0 1 5) peaks. (c) Scanning electron microscopy (SEM) image and (d) energy dispersive spectroscopy (EDS) maps of finely polished $Bi_{1.96}Ag_{0.04}Te_3$ pellet. Here BSE is abbreviated from backscattered electron. (e) SEM image and (f) EDS maps of finely polished $Bi_{1.96}Ag_{0.04}Te_3$ pellet taken from another site. (g) X-ray photoelectron spectroscopy (XPS) pattern of Ag3$d_{3/2}$ and Ag 3$d_{5/2}$ for $Bi_{1.96}Ag_{0.04}Te_3$ pellet. (h) SEM image of fractured $Bi_{1.96}Ag_{0.04}Te_3$ pellet.

successfully dope the Ag into the Bi_2Te_3 and study the doping mechanisms. Ag is commonly employed as an acceptor dopant to either improve the hole concentration n_p in p-type Bi_2Te_3-based thermoelectric materials or diminish the electron concentration n_e in n-type Bi_2Te_3-based materials. This strategic Ag doping allows for precise tuning of the n, consequently enhancing the S. Other prominent doping elements, such as Se, Cu, and In, are also known for their efficacy [55,56]. The doping mechanisms associated with these materials are centered around optimizing n and carrier mobility μ, thereby augmenting the $S^2\sigma$. Additionally, the introduction of lattice imperfections through doping serves to enhance phonon scattering, consequently reducing the κ. Therefore, effectively striking a balance among these factors can significantly enhance the ZT. During solvothermal synthesis, we use Bi_2O_3 and Na_2TeO_3 as precursors and Ag_2O as dopants, ethylene glycol (EG) as solvent, and adjust the doping level according to the stoichiometric ratio of Bi and Ag, as schematically shown in Fig. 1a. Fig. 1b illustrates the subsequent washing and sintering process for the synthesized Ag-doped Bi_2Te_3 powders. Detailed fabrication processes can be referred to Fig. S1 in the Supporting Information for reference. The as-synthesized powders needed to be dried and washed to remove the impurities followed by the fast spark plasma sintering (SPS) to sinter the powders into pellets. The composition of as-sintered pellets is then comprehensively investigated through X-ray photoelectron spectroscopy (XPS), X-ray diffraction (XRD), and energy dispersive spectroscopy (EDS), which demonstrated that Ag_{Bi} (Ag occupies Bi site) point defects have been successfully induced into Bi_2Te_3 matrix. These induced point defects optimize n to 1.53 × 10^{19} cm^{-3} and result in a high S of 204.33 μV K^{-1} at 298 K. Besides, by increasing the doping level, the precipitation of Ag_2Te with an n-type behavior is simultaneously observed, which promotes $S^2\sigma$ to 25.5 μW cm^{-1} K^{-2} at 298 K. The structural and morphological characterizations including XPS, XRD, scanning electron microscopy (SEM), and transmission electron microscopy (TEM) demonstrate that Ag-doping can induce localized crystal imperfections containing lattice distortions and dislocations, as illustrated in Fig. 1c.

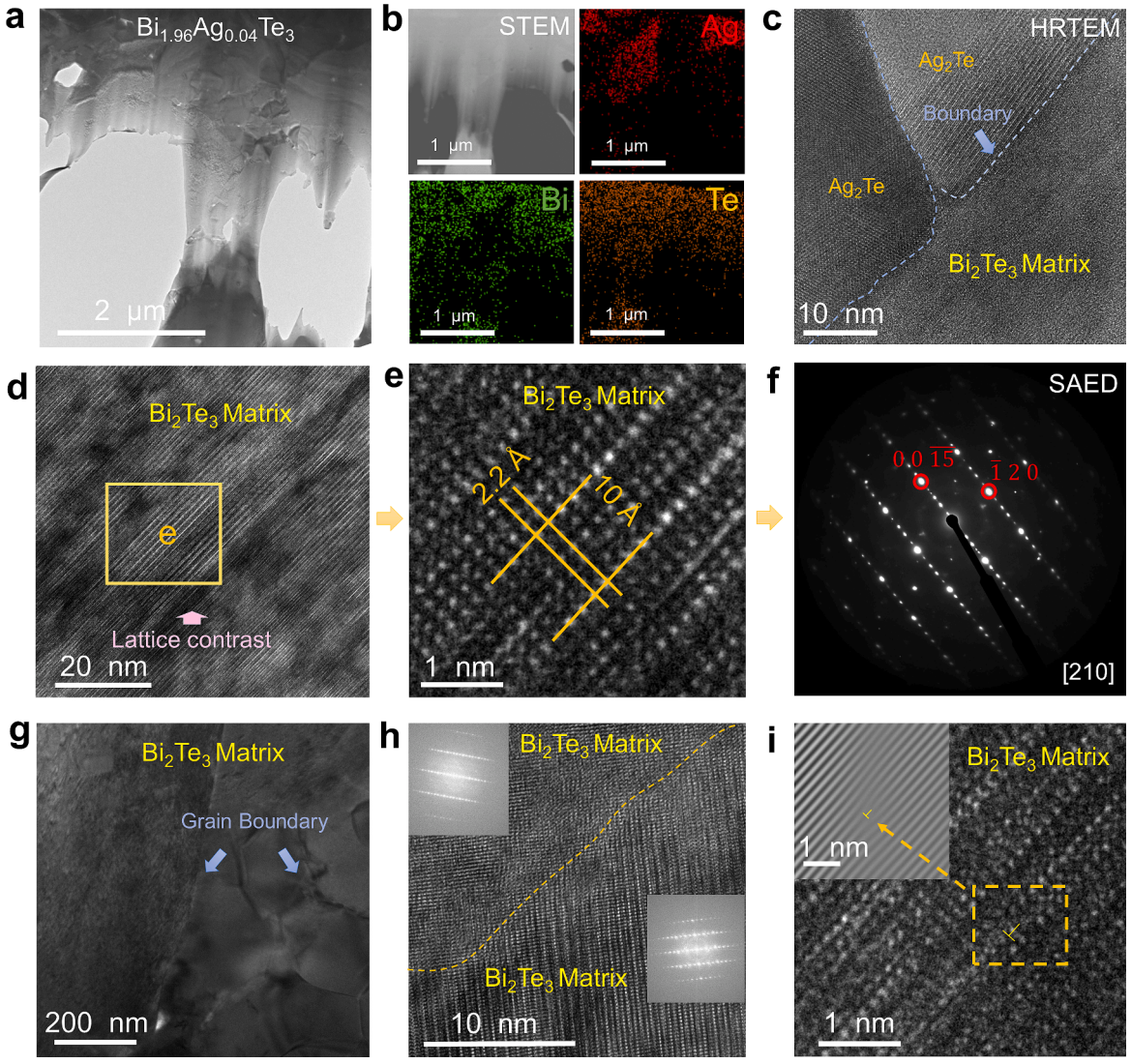

Fig. 3. Characterizations of nanostructure of solvothermally synthesized $Bi_{1.96}Ag_{0.04}Te_3$: (a) Low-magnification TEM image of lamella sample from bulk $Bi_{1.96}Ag_{0.04}Te_3$ through the focused ion beam (FIB) technique. (b) Corresponding STEM image and EDS maps for Bi, Te, and Ag elements. (c) HRTEM image of the phase boundaries between Bi_2Te_3 and Ag_2Te. (d) Magnified HRTEM image of Bi_2Te_3 matrix with significant lattice contrast. (e) Enlarged HRTEM image of Bi_2Te_3 matrix. (f) Corresponding selected area electron diffraction (SAED) pattern viewing along the (2 1 0) direction. (g) Magnified TEM image taken from another site for Bi_2Te_3 nanograins. (h) Corresponding magnified HRTEM image showing a typical grain boundary between the Bi_2Te_3 matrices, in which the nanograin on the right side is viewed along the [2 1 0] zone axis. (i) HRTEM image to show an edge-like dislocation. The corresponding inverse Fourier transform image is shown in the inset.

These lattice imperfections and the existence of Ag_2Te secondary phases further strengthen the phonon scattering, leading to a low κ_l of 0.41 W m^{-1} K^{-1} and in turn, promote the ZT to 1.03 at 298 K. Compared with previously reported n-type Bi_2Te_3-based materials synthesized by hydrothermal/solvothermal routes [32,45,57–59], our achieved ZT is highly competitive, as shown in Fig. 1d.

2. Result and discussion

In this work, we first solvothermally synthesized Ag-doped Bi_2Te_3 microplates (see Fig. S2), and then rationally sinter these microplates into polycrystalline bulk materials by an SPS technique. To carefully study the mechanism of solvothermally Ag-doping on improving the thermoelectric performance of Bi_2Te_3 and explore the best Ag doping concentration, we design our as-fabricated materials with nominal compositions of $Bi_{2-x}Ag_xTe_3$ (x = 0, 0.01, 0.02, 0.03, 0.04, 0.05). To characterize the structure and phase of the as-synthesized Ag-doped Bi_2Te_3, we performed XRD and EDS on bulk samples with different doping concentrations. Fig. 2a presents their XRD patterns, in which the 2θ ranges are all from 20° to 80°. The results indicate that all diffraction peaks can be indexed as trigonal-structured Bi_2Te_3 with a space group of $R\,\bar{3}\,m$, and the lattice parameters are a = 4.38 Å and c = 30.44 Å (PDF# 15-0863). With increasing doping concentration, diffraction peaks belonging to Ag_2Te precipitates can be observed due to the excessive doping limitation of Ag in Bi_2Te_3. Fig. 2b presents the magnified XRD patterns of (0 1 5) diffraction peaks in a 2θ range from 27.6° to 27.8°. With increasing doping level, the peak shifts to the lower 2θ due to the lattice expansion. Considering that the Ag has a larger ion size than Bi (Ag^+ = 1.15 Å and Bi^{3+} = 1.03 Å) [60], substituting Bi sites with Ag atoms can lead to a lattice expansion and in turn, the peak shift [37].

To investigate the composition, structure, and morphology of the solvothermally Ag-doped Bi_2Te_3, we performed SEM characterizations on bulk samples coupled with EDS. Fig. 2c presents an SEM image of a finely polished pellet with a nominal composition of $Bi_{1.96}Ag_{0.04}Te_3$, and Fig. 2d shows corresponding EDS maps including overlapping elements, Bi, Ag, and Te. Compared with other samples (Fig. S3), when the doping

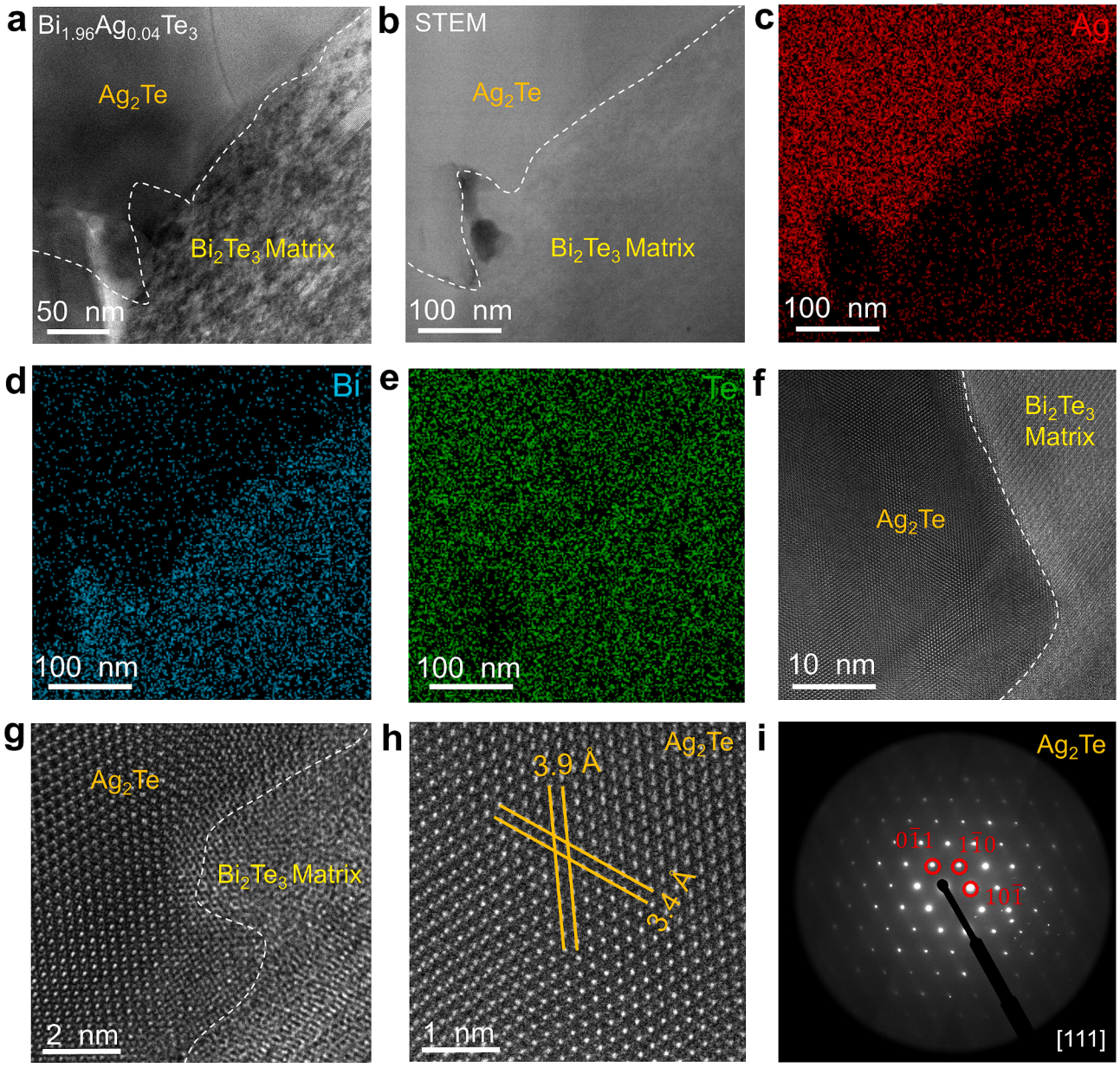

Fig. 4. Characterizations of nanostructure of Ag_2Te secondary phases: (a) TEM image of the phase boundaries between the Ag_2Te secondary phase and Bi_2Te_3 matrix. (b) Corresponding STEM image and EDS maps for (c) Ag, (d) Bi, and (e) Te elements. (f) Low- and (g) high-magnification HRTEM image to show the phase boundary between the Ag_2Te and Bi_2Te_3. (h) Enlarged HRTEM image of Ag_2Te secondary phase. (i) Corresponding selected area electron diffraction (SAED) pattern viewing along the [1 1 1] direction of Ag_2Te.

level x was >0.04, the Ag-rich precipitates can be observed and form the second phase of Ag_2Te due to the excessive doping limitation of Ag in Bi_2Te_3, which is in accordance with the XRD results. Fig. 2e-f present the SEM image and corresponding EDS maps of the $Bi_{1.96}Ag_{0.04}Te_3$ pellet taken from another area, from which one can see that all elements are uniformly distributed, indicating a homogenous Ag doping. These results evidence the presence of Bi, Te, Ag, and Ag_2Te secondary phases in the as-fabricated Ag-doped Bi_2Te_3 polycrystals. To identify the oxidation state of as-doped Ag in bulk Bi_2Te_3, Fig. 2g presents the XPS results of $Ag3d_{3/2}$ and Ag $3d_{5/2}$, indicating the existence of Ag^+, which is mainly from the point defects Ag_{Bi} and Ag_2Te secondary phases. Fig. 2h shows an SEM image of a fractured $Bi_{1.96}Ag_{0.04}Te_3$ pellet, from which one can see that most grains were along the same direction, indicating a strong anisotropy in the polycrystal structures. Similar results were found in pellets with other nominal compositions (Fig. S4), indicating that solvothermal synthesis is a good method to achieve the texturing effect [46].

To understand the nanostructure of the solvothermally Ag-doped Bi_2Te_3, we performed comprehensive TEM characterization of the $Bi_{1.96}Ag_{0.04}Te_3$ bulk materials, prepared using the focused ion beam (FIB) technique. Fig. 3a shows a low-magnification TEM image. Fig. 3b presents corresponding scanning TEM (STEM) image and EDS maps for Bi, Te, and Ag elements. As can be seen, some areas are Ag-rich and Bi-poor, indicating the potential existence of Ag_2Te secondary phases. Fig. 3c shows a high-resolution TEM (HRTEM) image taken from the interface between the Ag-rich area and normal area in Fig. 3b, in which the typical phase boundaries between the Ag_2Te and Bi_2Te_3 can be observed. For the Bi_2Te_3 matrix, Fig. 3d shows a magnified HRTEM image, in which significant lattice contrast can be observed, which is mainly caused by the point defects of Ag_{Bi} since the difference in ionic radius of Ag and Bi usually cause significant lattice strain. Fig. 3e presents a further magnified HRTEM image for the Bi_2Te_3 matrix viewed

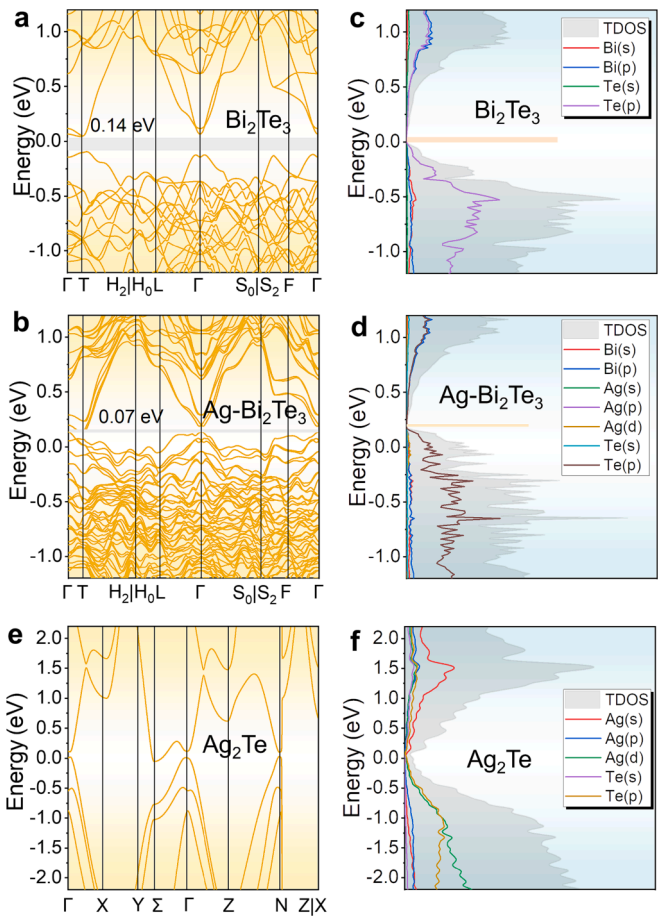

Fig. 5. Calculated band structures and DOSs for solvothermally Ag-doped Bi_2Te_3 through DFT calculations: Band structures of (a) Bi_2Te_3 ($Bi_{16}Te_{24}$) and (b) Ag-doped Bi_2Te_3 ($AgBi_{15}Te_{24}$). Corresponding DOSs of (c) Bi_2Te_3 ($Bi_{16}Te_{24}$) and (d) Ag-doped Bi_2Te_3 ($AgBi_{15}Te_{24}$). (e) Band structure and (f) Corresponding DOS of Ag_2Te.

along the [2 1 0] zone axis, which can be confirmed by the following selected area electron diffraction (SAED) pattern shown in Fig. 3f. Fig. 3e shows the interplanar spacing of 10 Å and 2.2 Å, corresponding to the interplanar spacing of the (00 $\overline{15}$) planes and ($\overline{1}$ 20) planes, respectively, further confirming the SAED results. Fig. 3g presents a magnified TEM image taken from another site, which shows several Bi_2Te_3 nanograins. Fig. 3h shows a magnified HRTEM image for a typical grain boundary between the Bi_2Te_3 matrices, in which the nanograin on the right side is viewed along the [2 1 0] zone axis. Fig. 3i shows a magnified HRTEM image with a dislocation containing an edge component, confirmed by the inset inverse Fourier transform image. Such dislocation may be caused by the formation of Ag_{Bi} by Ag-doping. The combination of these different types of lattice imperfections should effectively strengthen the scattering of phonons with different wavelengths and in turn, contribute to low κ_l.

To understand the nanostructure of the Ag_2Te secondary phase in the Bi_2Te_3 matrix, we performed detailed TEM characterizations. Fig. 4a presents a TEM image of a typical phase boundary between the Ag_2Te secondary phase and Bi_2Te_3 matrix, where different contrast can be observed between different phases. Fig. 4b shows a corresponding STEM image, and Fig. 4c-e present corresponding EDS maps for Bi, Te, and Ag elements, which confirm the existence of the Ag_2Te secondary phase in the Bi_2Te_3 matrix. The detailed line-scanning results for the element distributions can be seen in Fig. S5. Fig. 4f-g present the low- and high-magnification HRTEM images of a phase boundary between Ag_2Te and Bi_2Te_3, from which lattice mismatches can be clearly observed around the interface area, caused by the crystal structure difference between Ag_2Te and Bi_2Te_3. Such an incoherent interface is potentially effective in scattering phonons and in turn, suppressing κ_l. For the Ag_2Te secondary phase, Fig. 4h presents its HRTEM image, and Fig. 4i shows the corresponding SAED pattern. The results show that the image was taken along the [1 1 1] zone axis of Ag_2Te with measurable periodicities of interplanar spacing of 3.9 Å and 3.4 Å, which correspond to the interplanar spacing of the (10 $\overline{1}$) planes and (1 $\overline{1}$ 0) planes. The corresponding SAED pattern confirms the HRTEM results, indicating that the Ag_2Te is a tetragonal structure.

To understand the determined compositions and nanostructures, we further performed the first-principles density functional theory (DFT) calculations for Bi_2Te_3, Ag-doped Bi_2Te_3, and Ag_2Te, and the results are shown in Fig. 5 [61,62]. Fig. 5a-b compare the calculated band structures of Bi_2Te_3 ($Bi_{16}Te_{24}$) and Ag-doped Bi_2Te_3 ($AgBi_{15}Te_{24}$). As can be seen, Bi_2Te_3 has an intrinsic bandgap of 0.14 eV, exhibiting features of a typical narrow-gap semiconductor [63–65]. For Ag-dope Bi_2Te_3, it can be observed that the Fermi level shifts into the valence band, indicating that by doping with Ag^+ on Bi^{3+}, more hole carriers will be activated due to electron acceptor effect and switch the pristine n-type Bi_2Te_3 to p-type. Considering that there are high concentrations of Te vacancies in pristine Bi_2Te_3 synthesized by solvothermal synthesis (which is the reason why pristine Bi_2Te_3 exhibits typical n-type semiconducting behaviors), introducing rational Ag^+ on Bi^{3+} can potentially suppress the pristine high n_e and in turn, improve the thermoelectric performance [31]. However, over-doping Ag may lead to low n_e in n-type Bi_2Te_3 or even result in p-type Bi_2Te_3, therefore the doping concentration of Ag should be carefully determined, and this is why we determine nominal compositions of $Bi_{2-x}Ag_xTe_3$ by $x = 0$, 0.01, 0.02, 0.03, 0.04, and 0.05 in this work. Fig. 5c-d show the corresponding density of states (DOS) of Bi_2Te_3 ($Bi_{16}Te_{24}$) and Ag-doped Bi_2Te_3 ($AgBi_{15}Te_{24}$), indicating that Te_p contributes most to the valence bands, while both Te_p and Bi_p contribute most to the conduction band. For the secondary phase, Fig. 5e-f show the band structure and DOS of Ag_2Te, which exhibits a typical metallic behavior since Ag_2Te has no indirect bandgap but a direct bandgap. Therefore, the existence of the Ag_2Te secondary phase in the Bi_2Te_3 should have a positive effect on improving the overall n_e and thereby strengthening the σ.

To clarify the impact of solvothermally Ag doping on improving the thermoelectric performance of pristine Bi_2Te_3, we evaluated the main thermoelectric properties of $Bi_{2-x}Ag_xTe_3$ ($x = 0$, 0.01, 0.02, 0.03, 0.04, 0.05) from 298 K to 483 K, all along the directions perpendicular to the sintering pressure. Fig. 6a displays the temperature-dependent σ. With increasing the x to 0.03, σ was gradually decreased due to the release of hole carriers by Ag^+ substituting Bi^{3+}, which potentially suppresses n_e. When further increasing x from 0.03 to 0.05, σ increased due to the formation of metallic Ag_2Te secondary phases. Fig. 6b presents the temperature-dependent S. The negative value of S indicates that the semiconducting behavior of the $Bi_{2-x}Ag_xTe_3$ is n-type. By increasing x to 0.03, S increases gradually due to the release of hole carriers by Ag^+ substituting Bi^{3+}, which potentially suppresses n_e. However, when further increasing x from 0.03 to 0.05, S maintains at a high level, mainly due to the potential energy filtering effect triggered by the interfaces between metallic Ag_2Te secondary phases and Bi_2Te_3 matrix due to the significant difference in their band structures shown in Fig. 5. As a result, an outstanding $S^2\sigma$ of 25.5 μW cm^{-1} K^{-2} can be achieved at 298 K in the $Bi_{1.96}Ag_{0.04}Te_3$ pellet, as shown in Fig. 6c.

To prove the discussions above, n_e and μ of $Bi_{2-x}Ag_xTe_3$ ($x = 0$, 0.01, 0.02, 0.03, 0.04, 0.05) were evaluated at room temperature, as shown in Fig. 6d. By increasing x to 0.03, n_e was decreased gradually due to the release of hole carriers by Ag^+ substituting Bi^{3+}, confirming the drop of σ. With further increasing x from 0.03 to 0.05, n_e increases due to the formation of metallic Ag_2Te secondary phases, explaining the rise of σ. With increasing x to 0.03, μ was increased gradually due to the decrease of n_e. With further increasing the x from 0.03 to 0.04, there is a slight

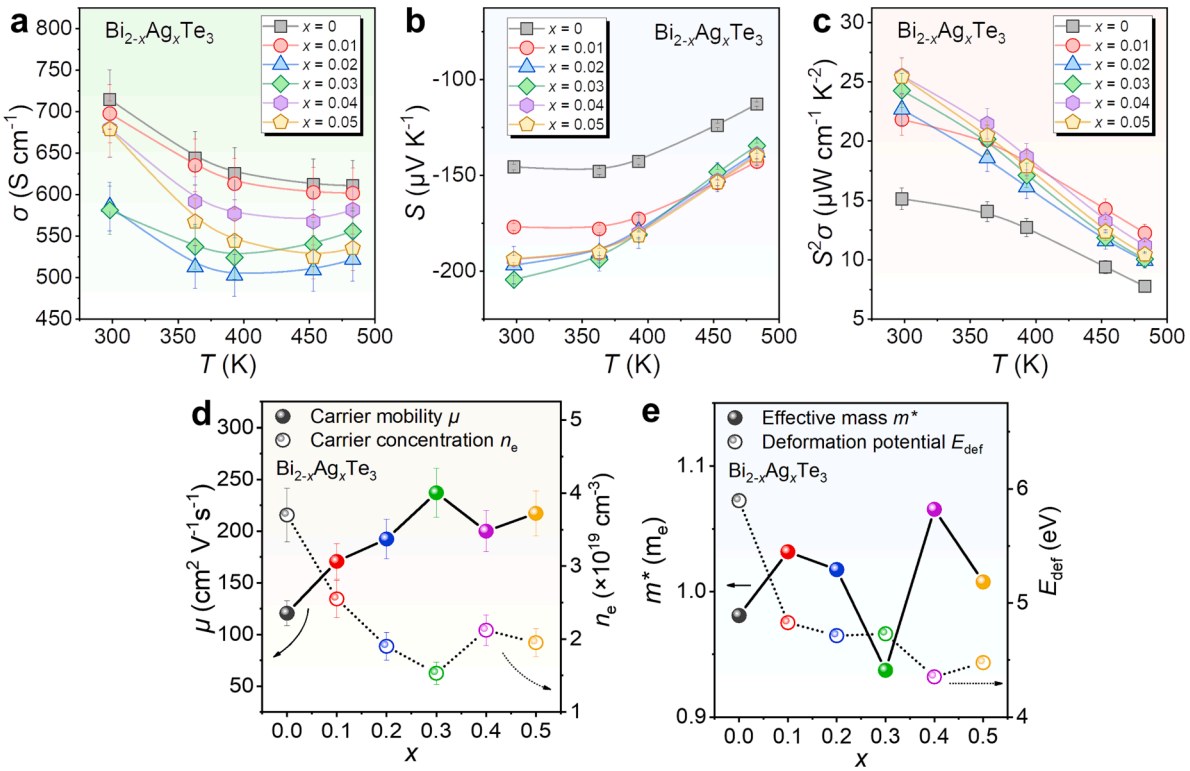

Fig. 6. Evaluation of thermoelectric performance of solvothermally synthesized Ag-doped Bi_2Te_3 pellets with nominal compositions of $Bi_{2-x}Ag_xTe_3$ (x = 0, 0.01, 0.02, 0.03, 0.04, 0.05): Temperature-dependent of (a) σ, (b) S, and (c) $S^2\sigma$ values. (d) Measured room-temperature n_e and μ. (e) Calculated room-temperature m^* and E_{def} by the SPB model.

drop in μ, which is mainly derived from the formation of Ag_2Te secondary phases due to the carrier scattering at the as-induced phase boundaries. Further increasing x from 0.04 to 0.05 resulted in increased μ again, mainly owing to the slight decrease of n_e. Fig. 6e compares the calculated effective mass m^* and deformation potential E_{def} as functions of x based on the single parabolic band (SPB) model. As can be seen, m^* was first increased and then significantly decreased when x was from 0 to 0.03, which is mainly caused by the drop of n_e. When $x = 0.04$, Ag_2Te secondary phases were formed, and m^* was significantly boosted, which is direct evidence of the triggered energy filtering effect at the interfaces between metallic Ag_2Te secondary phases and Bi_2Te_3 matrix, explaining the retained high S due to the energy filtering effect that effectively filters the low-energy carriers [28]. With increasing the Ag doping level, E_{def} decreases gradually due to the variation in the overall anisotropy of the entire polycrystal material (texturing effect). The E_{def} is related to free electrons and the local lattice deformation [66,67]. With the increase of the doping level, the introduced lattice deformation is increased, but the n_e is decreased, so the effective potential generated by the lattice deformation is decreased with the doping level. In addition to that, the increase in doping level gradually changes the properties of Bi_2Te_3 nanoplates, which enhances the anisotropy of Bi_2Te_3 nanoplates. When the doping limit is exceeded, the E_{def} is suddenly increased due to the massive change of the texturing inside the materials, which is caused by the generation of the secondary phase. After further increasing the doping level, although the n_e is further increased, the lattice deformation that can be introduced has been saturated, so the E_{def} is reduced again.

In terms of the thermal transport performance of $Bi_{2-x}Ag_xTe_3$ (x = 0, 0.01, 0.02, 0.03, 0.04, 0.05), the temperature-dependent κ were evaluated, as shown in Fig. 7a. The κ values were calculated by the formula $\kappa = D \times C_p \times \rho$, where D is the measured thermal diffusivity (Fig. S6a), ρ is the measured mass density (Fig. S6b), and C_p is the specific heat capacity. Generally, with increasing x, κ was decreased due to the increased density of crystal/lattice imperfections in the materials. κ is comprised of κ_l and κ_e. κ_e can be obtained by $\kappa_e = \sigma LT$ based on the Wiedemann-Franz law [31], in which L is the Lorentz number determined from the SPB model (Fig. S6c). κ_e exhibits the same trends as σ (Fig. S6d) [2,68]. Fig. 7b presents the temperature-dependent κ_l with different Ag doping levels by $\kappa_l = \kappa - \kappa_e$. As can be seen, the lowest κ_l of 0.41 W m^{-1} K^{-1} can be obtained from the $Bi_{1.96}Ag_{0.04}Te_3$ at room temperature. Such suppressed κ_l mostly benefits from strong phonon scattering, which is induced by the observed lattice imperfections including point defects, grain boundaries, local lattice distortions, and dislocations. Additionally, the presence of the second phase of Ag_2Te can introduce the grain-boundary dislocation strain, which can further enhance phonon scattering and thereby reduce the κ_l. It should be noted that when the amount of Ag_2Te secondary phase is excessive ($x = 0.05$), the κ_l is increased, mainly due to the metallic thermal transport behavior of Ag_2Te. The κ of Ag_2Te is around 0.9 ~ 1.1 W m^{-1} K^{-1} at room temperature [69,70]. The κ of Ag_2Te increases with the temperature, indicating the typical metallic thermal transport behavior [69,70]. Also, as shown by the band structure and DOS of Ag_2Te (Fig. 5e-f), Ag_2Te has no indirect bandgap but has a direct bandgap, double-confirming a typical metallic behavior. It is worth mentioning that when the temperature exceeds 425 K, the κ of Ag_2Te will decrease sharply due to the phase transition. Therefore, a rational concentration of the Ag_2Te secondary phase is of significance.

Fig. 7c displays the determined temperature-dependent ZT for $Bi_{2-x}Ag_xTe_3$ (x = 0, 0.01, 0.02, 0.03, 0.04, 0.05), in which a maximum ZT values of 1.03 can be achieved at 298 K for the $Bi_{1.96}Ag_{0.04}Te_3$ pellet. The as-achieved ZT is significantly improved by 202 % compared with the undoped Bi_2Te_3 pellet, indicating great potential for practical room-temperature applications. Fig. 7d presents the comparison of the predicted ZT by the SPB model and measured ZT as a function of n_e [63,71]. A slightly higher ZT of 1.14 can be further achieved by finely tuning the n_e to 1.2 × 10^{19} cm^{-3}. As can be seen, the n_e has been considerably optimized to the best value by solvothermally Ag doping. Therefore,

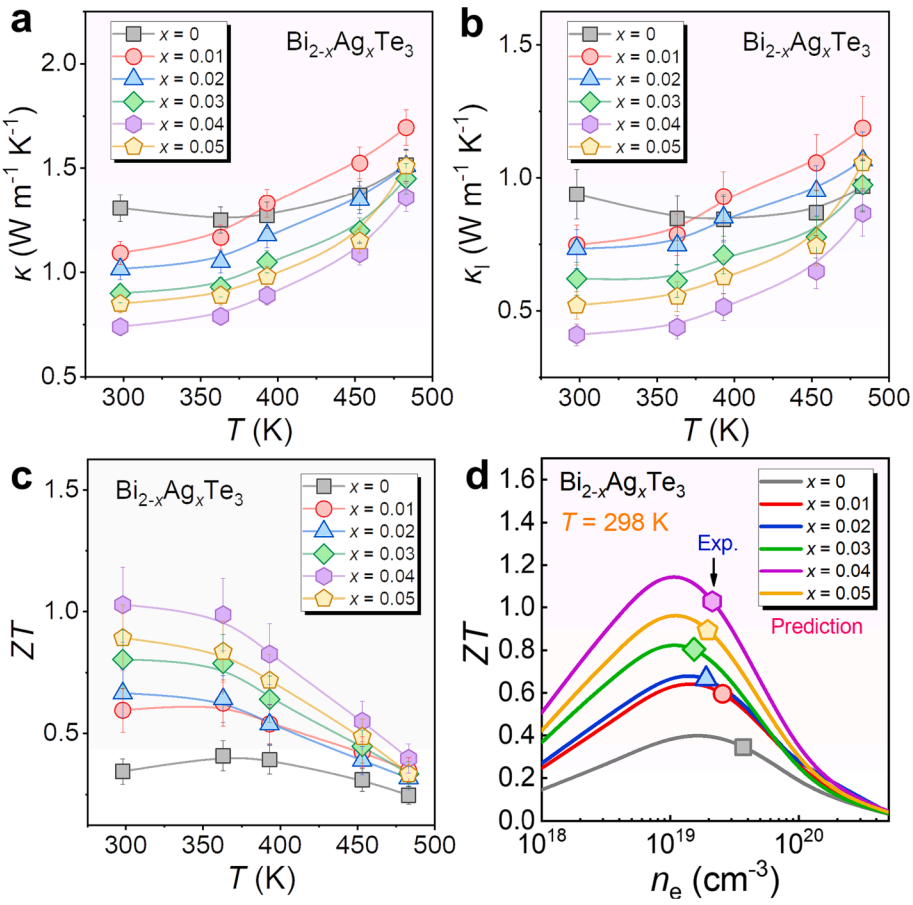

Fig. 7. Temperature-dependent (f) κ, (g) κ_l, and (h) ZT values. (i) Comparison of predicted ZT by the SPB model and measured ZT as a function of n_e.

further suppressing the κ_l should be a good direction to enhance the ZT value.

3. Conclusion

In summary, we adopt a facile solvothermal synthesis route to achieve Ag doping in n-type Bi_2Te_3 and explore the unique doping mechanism. Detailed micro/nanostructural characterizations and calculations confirm that Ag_{Bi} rationally tunes the n_e while the as-formed Ag_2Te nanophases effectively trigger the energy filtering effect to maintain a high S while keeping a high σ, thereby contributing to a competitively high $S^2\sigma$ of 25.5 μW cm^{-1} K^{-2} at 298 K. Additionally, the observed various lattice imperfections including point defects, grain boundaries/interfaces, local lattice distortions, and dislocations induced by solvothermally Ag doping further strengthen the phonon scattering and thereby, reducing the κ to 0.74 W m^{-1} K^{-1} and in turn, boosting the ZT to 1.03 at 298 K. This work fills the gap of solvothermally Ag-doping mechanism in Bi_2Te_3 and provide a guidance for designing high-performing thermoelectric materials.

4. Experimental section

The experimental details can be seen in the Supporting Information.

Declaration of Competing Interest

The authors declare that they have no known competing financial interests or personal relationships that could have appeared to influence the work reported in this paper.

Data availability

Data will be made available on request.

Acknowledgments

This work was financially supported by the Australian Research Council, UQ-HBIS Innovation Center for Sustainable Steel Project, and QUT Capacity Building Professor Program. The Australian Microscopy & Microanalysis Research Facility is acknowledged for providing characterization facilities. Research Computing Centre in University of Queensland and National Computational Infrastructure supported by Australian Government are acknowledged for providing computing facilities.

Appendix A. Supplementary data

Supplementary data to this article can be found online at https://doi.org/10.1016/j.cej.2023.146428.

References

[1] Y. Zhang, S. Hao, L.-D. Zhao, C. Wolverton, Z. Zeng, J. Mater. Chem. A 4 (2016) 12073–12079.
[2] J. He, T.M. Tritt, Science 357 (2017) eaak9997.
[3] T.-R. Wei, M. Jin, Y. Wang, H. Chen, Z. Gao, K. Zhao, P. Qiu, Z. Shan, J. Jiang, R. Li, L. Chen, J. He, X. Shi, Science 369 (2020) 542.
[4] S. Roychowdhury, T. Ghosh, R. Arora, M. Samanta, L. Xie, K. Singh Niraj, A. Soni, J. He, V. Waghmare Umesh, K. Biswas, Science 371 (2021) 722–727.
[5] W.-Y. Chen, X.-L. Shi, J. Zou, Z.-G. Chen, Small Methods 6 (2022) 2101235.
[6] Z.-H. Zheng, X.-L. Shi, D.-W. Ao, W.-D. Liu, M. Li, L.-Z. Kou, Y.-X. Chen, F. Li, M. Wei, G.-X. Liang, P. Fan, G.Q. Lu, Z.-G. Chen, Nat. Sustain. 6 (2023) 180–191.
[7] X.-L. Shi, J. Zou, Z.-G. Chen, Chem. Rev. 120 (2020) 7399–7515.

[8] Z. Chen, X. Zhang, Y. Pei, Adv. Mater. 30 (2018) 1705617.
[9] W.-Y. Chen, X.-L. Shi, J. Zou, Z.-G. Chen, Mat. Sci. Eng. R 151 (2022), 100700.
[10] L.-Y. Lou, J. Yang, Y.-K. Zhu, H. Liang, Y.-X. Zhang, J. Feng, J. He, Z.-H. Ge, L.-D. Zhao, Adv. Sci. 9 (2022) 2203250.
[11] C. Xing, Y. Zhang, K. Xiao, X. Han, Y. Liu, B. Nan, M.G. Ramon, K.H. Lim, J. Li, J. Arbiol, B. Poudel, A. Nozariasbmarz, W. Li, M. Ibáñez, A. Cabot, ACS Nano 17 (2023) 8442–8452.
[12] Z. Zhang, K. Zhao, T.-R. Wei, P. Qiu, L. Chen, X. Shi, Energ. Environ. Sci. 13 (2020) 3307–3329.
[13] S. Chandra, P. Dutta, K. Biswas, ACS Nano 16 (2022) 7–14.
[14] X.-L. Shi, X. Tao, J. Zou, Z.-G. Chen, Adv. Sci. 7 (2020) 1902923.
[15] B. Qin, D. Wang, T. Hong, Y. Wang, D. Liu, Z. Wang, X. Gao, Z.-H. Ge, L.-D. Zhao, Nat. Commun. 14 (2023) 1366.
[16] M. Hong, J. Zou, Z.G. Chen, Adv. Mater. 31 (2019) 1807071.
[17] M. Hong, Z.-G. Chen, Accounts. Chem. Res. 55 (2022) 3178–3190.
[18] X. Zhang, Z. Bu, S. Lin, Z. Chen, W. Li, Y. Pei, Joule 4 (2020) 986–1003.
[19] B. Jia, Y. Huang, Y. Wang, Y. Zhou, X. Zhao, S. Ning, X. Xu, P. Lin, Z. Chen, B. Jiang, J. He, Energ. Environ. Sci. 15 (2022) 1920–1929.
[20] Z.-Z. Luo, S. Cai, S. Hao, T. Bailey, Y. Luo, W. Luo, Y. Yu, C. Uher, C.M. Wolverton, V. Dravid, Z. Zou, Q. Yan, M.G. Kanatzidis, Energ. Environ. Sci. 15 (2022) 368–375.
[21] C. Qin, L. Cheng, Y. Xiao, C. Wen, B. Ge, W. Li, Y. Pei, Mater. Today Phys. 17 (2021), 100355.
[22] L. Li, W.-D. Liu, Q. Liu, Z.-G. Chen, Adv. Funct. Mater. 32 (2022) 2200548.
[23] Y. Jia, Q. Jiang, H. Sun, P. Liu, D. Hu, Y. Pei, W. Liu, X. Crispin, S. Fabiano, Y. Ma, Y. Cao, Adv. Mater. 33 (2021) 2102990.
[24] Q. Li, Z. Cao, H. Cheng, J. Zhang, Z. Ma, W. Wahyudi, L. Cavallo, Q. Sun, J. Ming, ACS Mater. Lett. 4 (2022) 2469–2479.
[25] H. Xue, Y. Wu, Z. Wang, Y. Shen, Q. Sun, G. Liu, D. Yin, L. Wang, Q. Li, J. Ming, ACS Appl. Mater. Interfaces 13 (2021) 40471–40480.
[26] L. Zhou, J. Zhang, Y. Wu, W. Wang, H. Ming, Q. Sun, L. Wang, J. Ming, H. N. Alshareef, Adv. Energy Mater. 9 (2019) 1902194.
[27] T. Cao, X.-L. Shi, Z.-G. Chen, Prog. Mater Sci. 131 (2023), 101003.
[28] I.T. Witting, T.C. Chasapis, F. Ricci, M. Peters, N.A. Heinz, G. Hautier, G.J. Snyder, Adv. Electron. Mater. 5 (2019) 1800904.
[29] S.A. Nemov, Y.V. Ulashkevich, A.A. Rulimov, A.E. Demchenko, A.A. Allahkhah, I. V. Sveshnikov, M. Dzhafarov, Semiconductors+ 53 (2019) 603–606.
[30] M. Tan, W.-D. Liu, X.-L. Shi, Q. Sun, Z.-G. Chen, Appl. Phys. Rev. 10 (2023), 021404.
[31] Y. Wang, W.-D. Liu, X.-L. Shi, M. Hong, L.-J. Wang, M. Li, H. Wang, J. Zou, Z.-G. Chen, Chem. Eng. J. 391 (2019), 123513.
[32] F. Ghafoor, B. Ghafoor, D.-K. Kim, M.F. Khan, M. Anis-ur-Rehman, J. Mater. Res. Technol. 23 (2023) 3617–3625.
[33] H.-J. Wu, W.-T. Yen, Acta Mater. 157 (2018) 33–41.
[34] C.-H. Lin, W.-T. Yen, Y.-F. Tsai, H.-J. Wu, ACS Appl. Energy Mater. 3 (2020) 1311–1318.
[35] H.-J. Wu, B.-Y. Chen, H.-Y. Cheng, Acta Mater. 122 (2017) 120–129.
[36] Y. Wu, R. Zhai, T. Zhu, X. Zhao, Mater. Today Phys. 2 (2017) 62–68.
[37] W.-T. Yen, H.-C. Huang, K.-K. Wang, H.-J. Wu, Mater. Today Phys. 19 (2021), 100416.
[38] X. Yan, B. Poudel, Y. Ma, W.S. Liu, G. Joshi, H. Wang, Y. Lan, D. Wang, G. Chen, Z. F. Ren, Nano Lett. 10 (2010) 3373–3378.
[39] L. Hu, H. Wu, T. Zhu, C. Fu, J. He, P. Ying, X. Zhao, Adv. Energy Mater. 5 (2015) 1500411.
[40] L. Hu, T. Zhu, X. Liu, X. Zhao, Adv. Funct. Mater. 24 (2014) 5211–5218.
[41] Y. Min, J.W. Roh, H. Yang, M. Park, S.I. Kim, S. Hwang, S.M. Lee, K.H. Lee, U. Jeong, Adv. Mater. 25 (2013) 1425–1429.
[42] Y. Min, G. Park, B. Kim, A. Giri, J. Zeng, J.W. Roh, S.I. Kim, K.H. Lee, U. Jeong, ACS Nano 9 (2015) 6843–6853.
[43] Q. Tao, H. Wu, W. Pan, Z. Zhang, Y. Tang, Y. Wu, R. Fan, Z. Chen, J. Wu, X. Su, X. Tang, ACS Appl. Mater. Interfaces 13 (2021) 60216–60226.
[44] C.-H. Kuo, C.-S. Hwang, M.-S. Jeng, W.-S. Su, Y.-W. Chou, J.-R. Ku, J. Alloy. Compd. 496 (2010) 687–690.
[45] K. Ahn, J.K. Won, Y.K. Kang, C. Hwang, I. Chung, M.-G. Kim, Curr. Appl Phys. 19 (2019) 97–101.
[46] J. Yuan, X.-L. Shi, D.-Z. Wang, W.-D. Liu, M. Li, W. Chen, Q. Yang, Y. Wang, Q. Liu, Z.-G. Chen, ACS Appl. Energy Mater. 6 (2023) 6227–6236.
[47] H. Mamur, M.R.A. Bhuiyan, F. Korkmaz, M. Nil, Renew. Sust. Energ. Rev. 82 (2018) 4159–4169.
[48] Y. Kimura, R. Mori, S. Yonezawa, H. Yabuki, H. Namiki, Y. Ota, M. Takashiri, Sci. Rep. 10 (2020) 6315.
[49] N. Nandihalli, D.H. Gregory, T. Mori, Adv. Sci. 9 (2022) 2106052.
[50] M. Hong, Z.-G. Chen, J. Zou, Chin. Phys. B 27 (2018), 048403.
[51] J. Pei, B. Cai, H.-L. Zhuang, J.-F. Li, Natl. Sci. Rev. 7 (2020) 1856–1858.
[52] T. Cao, X.-L. Shi, M. Li, B. Hu, W. Chen, W.-D. Liu, W. Lyu, J. MacLeod, and Z.-G. Chen, eScience 3 (2023) 100122.
[53] M. Hong, Z.-G. Chen, L. Yang, T.C. Chasapis, S.D. Kang, Y. Zou, G.J. Auchterlonie, M.G. Kanatzidis, G.J. Snyder, J. Zou, J. Mater. Chem. A 5 (2017) 10713–10721.
[54] L. Yang, Z.-G. Chen, G. Han, M. Hong, L. Huang, J. Zou, J. Mater. Chem. A 4 (2016) 9213–9219.
[55] M. Hong, T.C. Chasapis, Z.-G. Chen, L. Yang, M.G. Kanatzidis, G.J. Snyder, J. Zou, ACS Nano 10 (2016) 4719–4727.
[56] X. Bai, M. Ji, M. Xu, N. Su, J. Zhang, J. Wang, C. Zhu, Y. Yao, B. Li, Inorg. Chem. Front. 6 (2019) 1097–1102.
[57] M. Yaprintsev, A. Vasil'ev, O. Ivanov, J. Alloy. Compd. 900 (2022), 163516.
[58] J. Chen, D. Bao, Q. Sun, W.-D. Liu, C. Liu, J. Tang, L. Yang, D. Zhou, M.S. Dargusch, Z.-G. Chen, J. Solid State Chem. 296 (2021), 121987.
[59] K. Rani, V. Gupta, Ranjeet, A. Pandey, J. Mater. Sci. Mater. El. 34 (2023) 1074.
[60] S.S. Batsanov, Acta Crystallogr. Sect. B: Struct. Sci. Crystal Eng. Mater. 76 (2020) 38–40.
[61] E.V. Shah, D.R. Roy, Comp. Mater. Sci. 88 (2014) 156–162.
[62] K.T. Kim, T.S. Min, S.-D. Kim, E.-A. Choi, D.W. Kim, S.-Y. Choi, Nano Energy 55 (2019) 486–493.
[63] I.T. Witting, F. Ricci, T.C. Chasapis, G. Hautier, G.J. Snyder, Research 2020 (2020) 4361703.
[64] C. Zhang, X. Geng, B. Chen, J. Li, A. Meledin, L. Hu, F. Liu, J. Shi, J. Mayer, M. Wuttig, O. Cojocaru-Mirédin, Y. Yu, Small 17 (2021) 2104067.
[65] H.-S. Kim, N.A. Heinz, Z.M. Gibbs, Y. Tang, S.D. Kang, G.J. Snyder, Mater. Today 20 (2017) 452–459.
[66] K. Watanabe, T. Nagata, Y. Wakayama, T. Sekiguchi, R. Erdélyi, J. Volk, ACS Nano 9 (2015) 2989–3001.
[67] Z. Li, P. Graziosi, N. Neophytou, Phys. Rev. B 104 (2021), 195201.
[68] T. Zhu, Y. Liu, C. Fu, J.P. Heremans, J.G. Snyder, X. Zhao, Adv. Mater. 29 (2017) 1605884.
[69] V. Sharma, D. Sharma, R. Bhatt, P.K. Patro, G.S. Okram, ACS Appl. Energy Mater. 5 (2022) 13887–13894.
[70] H. Hu, K. Xia, Y. Wang, C. Fu, T. Zhu, X. Zhao, J. Mater. Sci. Technol. 91 (2021) 241–250.
[71] P. Devender, A. Gehring, A. Gaul, K. Hoyer, R.J. Vaklinova, M. Mehta, T. Burghard, D.J. Borca-Tasciuc, K.K. Singh, G. Ramanath, Adv. Mater. 28 (2016) 6436–6441.